44th AIAA Aerospace Sciences Meeting and Exhibit
9 - 12 January 2006, Reno, Nevada

AIAA 2006-877

Simulations of Flow Separation Control using Plasma Actuators

Y. B. Suzen*
North Dakota State University, Fargo, ND 58105

P. G. Huang†
University of Kentucky, Lexington, KY 40506

A mathematical model was developed for plasma actuators used in flow control applications. The effects of the plasma actuators on the external flow are incorporated into Navier Stokes computations as a body force vector, which is given as a product of the net charge density and the electric field. The model computes this body force vector by solving two additional equations: one for the electric field due to the applied AC voltage at the electrodes and the other for the charge density representing the ionized air. The details of model development, initial model calibration, and validation using available experimental data are presented. The effects of plasma actuator on control of flow separation on a PAK-B blade are demonstrated numerically.

Nomenclature

C_p	=	pressure coefficient
C_x	=	axial chord for Pak-B blade
e	=	elementary charge, C
$\vec{E}$	=	electric field, N/C
ε	=	permittivity, $\varepsilon = \varepsilon_r \varepsilon_o$
ε_r	=	relative permittivity
ε_o	=	permittivity of free space, 8.854×10^{-12} C^2/Nm^2
$\vec{f}_B$	=	body force vector, N/m^3
FSTI	=	freestream turbulence intensity, %
Φ	=	total electric potential, Volt, $\Phi = \phi + \varphi$
ϕ	=	electric potential due to external electric field, Volt
φ	=	electric potential due to net charge density, Volt
k	=	Boltzmann's constant
L_e	=	length of the electrode
λ_d	=	Debye length, m
μ	=	location parameter for Gaussian distribution
n_i	=	ion density in the plasma
n_e	=	electron density in the plasma
n_o	=	background plasma density
ω	=	frequency, Hz
Re	=	Reynolds number based on inlet velocity and axial chord
ρ_c	=	net charge density, C/m^3

*Assistant Professor, Department of Mechanical Engineering and Applied Mechanics, 108 Dolve Hall, bora.suzen@ndsu.edu, Senior Member AIAA.
†Professor and Director of Graduate Studies, Department of Mechanical Engineering, 151 RGAN Bldg., ghuang@engr.uky.edu, Senior Member AIAA.

σ	=	scale parameter for Gaussian distribution
t	=	time, s
T	=	temperature of the species
U_{in}	=	inlet velocity
U	=	streamwise velocity
x, y	=	coordinates
y_n	=	wall normal distance

I. Introduction

The use of plasma actuators for active flow control has been demonstrated to be an effective method in several flow-control-related applications including flow separation and boundary layer control. The plasma actuators consist of two electrodes that are located on a surface separated by a dielectric material as shown in Fig. 1. A high-voltage AC supplied to the electrodes causes the air in their vicinity to weakly ionize. The ionized air (plasma), in the presence of the electric field gradient produced by the electrodes, result in a body force vector acting on the external flow that can induce steady or unsteady velocity components. The effectiveness of plasma actuators in controlling flow separation has been demonstrated by several researchers [1-9]. These experiments showed that a range of parameters have to be taken into consideration for effective flow control including the location of the actuators on the surface, orientation, size, and relative placement of the embedded and exposed electrodes, applied voltage, and frequency of the actuation. Due to a large number of parameters involved, optimizing the performance of actual applications can be a fairly complicated task. CFD simulations can provide a useful tool in design and optimization of such complex flow control systems.

Computational studies of plasma flow control have been limited in comparison to the vast number of

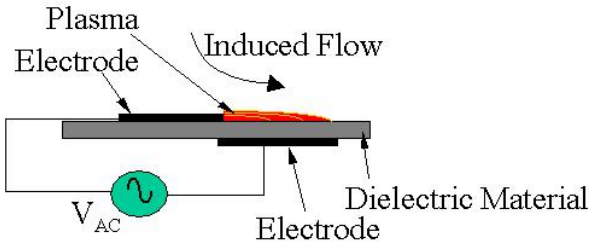

Figure 1. Schematic of plasma actuator.

experimental studies reported[10-14]. Recently, the authors developed a new robust numerical simulation methodology for active flow separation control applications using plasma actuators[15]. In this new approach, the effect of the plasma actuators on the external flow is incorporated into Navier Stokes computations as a body force vector. The body force is obtained as a product of the net charge density and the electric field. The new model solves the Maxwell equation to obtain the electric field due to the applied AC voltage at the electrodes and an additional equation for the charge density representing the plasma density. In this paper, details of the model development and implementation are described and the model is employed in computations of flow separation control over a PAK-B blade. The model is summarized in the next section.

II. Modeling Plasma Actuator Physics in CFD Computations

The body force that the plasma actuator induces on the external flow can be expressed in terms of the applied voltage and incorporated into the Navier Stokes equations. By neglecting magnetic forces, the electrohydrodynamic (EHD) force can be expressed as

$$\vec{f}_B = \rho_c \vec{E} \tag{1}$$

where, $\vec{f}_B$ is the body force per unit volume, ρ_c is net the charge density and $\vec{E}$ is the electric field. If the time variation of the magnetic field is negligible, as is often the case in plasma, the Maxwell's equations give rise to $\nabla \times E \approx 0$. This implies that the electric field can be derived from the gradient of a scalar potential[16]:

$$\vec{E} = -\nabla \Phi. \tag{2}$$

Gauss's law yields:

$$\nabla \cdot (\varepsilon \vec{E}) = \rho_c \tag{3}$$

or

$$\nabla \cdot (\varepsilon \nabla \Phi) = -\rho_c \tag{4}$$

where ε is the permittivity. The permittivity can be expressed as:

$$\varepsilon = \varepsilon_r \varepsilon_o \tag{5}$$

where ε_r is the relative permittivity of the medium, and ε_o is the permittivity of free space.

If we write the net charge density within the plasma at any point in terms of the elementary charge *e*, the background plasma density n_o, the temperature of the species *T*, and introduce the Debye length λ_d the charge density can be expressed in terms of the potential Φ and the Debye length λ_d [16],

$$\rho_c / \varepsilon_o = (-1/\lambda_d^2)\Phi \tag{6}$$

The body force given by Eq. (1) can be calculated using Eqs. (2) and (6) by imposing the applied voltage at the electrodes as boundary conditions on Φ as shown in Figs. 2a and 2b.

Experiments indicate that independent of which electrode the voltage is applied to, and independent of the polarity of the applied voltage, the resultant body force and therefore the induced flow is in the direction towards the embedded electrode, that is, to the right in Figs. 2. However, if the equations (2) and (6) are used in their current forms there are instances where the body force is directed in the negative direction causing the flow to move in the

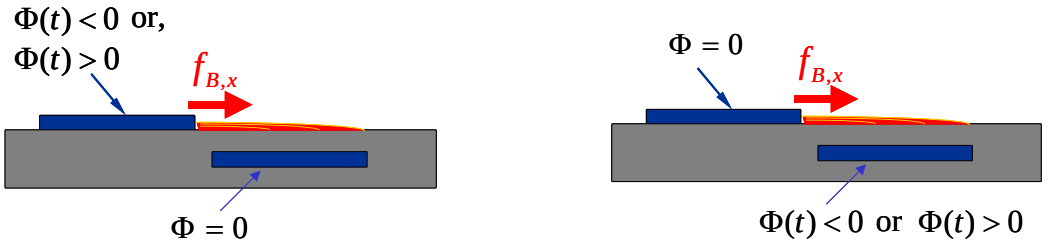

(a) Voltage applied at the upper electrode **(b) Voltage applied at the lower electrode**

Figure 2. Experimentally observed body force and flow directions.

same direction. In Fig. 3a, it can be seen that when the voltage applied at the exposed electrode is positive and the embedded electrode is grounded, $\partial\Phi/\partial x$ becomes negative. As a result, the *x* component of the electric field E_x is positive. From Eq. 6, we deduce $\rho_c < 0$ because $\Phi > 0$. Finally Eq. 1 results in a negative value of $f_{b,x}$. This outcome is in contradiction to the experimental observation. A similar analysis of the case when negative voltage is applied at the embedded electrode as shown in Fig. 3b also results in the same wrong predicted behavior.

The remedy we propose to this problem is to decompose the electric potential into two parts by using the superposition technique [15]. Since the gas particles are weakly ionized, we can assume the potential Φ can be decoupled into two parts: one being a potential due to the external electric field, ϕ, and the other being a potential

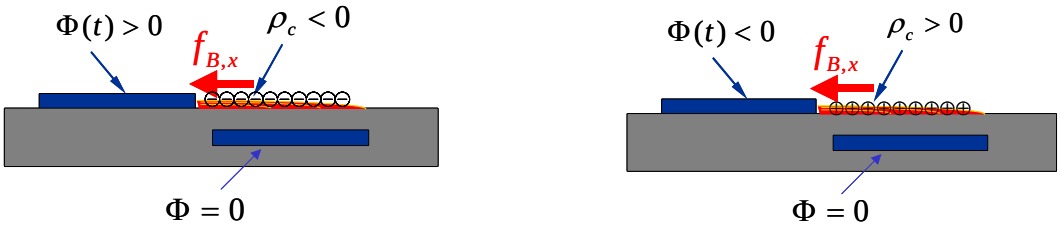

(a) Positive voltage at the upper electrode **(b) Negative voltage at the upper electrode**

Figure 3. Body force and flow directions using Eqs. (2) and (6).

due to the net charge density in the plasma, φ,

$$\Phi = \phi + \varphi. \tag{7}$$

This approach is similar to the one used in numerical simulation of electroosmotic flows in which case the external electric field generates a force on the charged particles creating flow[17].

If we assume that the Debye thickness is small and the charge on the wall is not large, the distribution of charged species in the domain is governed by the potential caused by the electric charge on the wall and is largely unaffected

by the external electric field. Therefore, we can write two independent equations in terms of these two potentials, one for the external electric field due to the applied voltage at the electrodes:

$$\nabla \cdot (\varepsilon_r \nabla \phi) = 0 \tag{8}$$

and another one for the potential due to the charged particles:

$$\nabla \cdot (\varepsilon_r \nabla \varphi) = -(\rho_c / \varepsilon_o). \tag{9}$$

Using $\rho_c / \varepsilon_o = \left(-1/\lambda_d^2\right)\varphi$ Eq. (9) can be written as[16],

$$\nabla \cdot (\varepsilon_r \nabla \rho_c) = \rho_c / \lambda_d^2. \tag{10}$$

Eq. (8) provides the solution for the electric potential, ϕ, using the applied voltage on the electrodes as boundary conditions and ρ_c is obtained from Eq. (10) with a prescribed boundary condition on the surface over the embedded electrode. The boundary condition is synchronized with the applied voltage on the electrode and the resultant body force vector is computed by

$$\vec{f}_B = \rho_c \vec{E} = \rho_c(-\nabla \phi). \tag{11}$$

Using Eqs. (8), (10), and (11) the body force is always directed in the experimentally observed direction as illustrated in Figs. 4a and 4b. In Fig. 4a, when the voltage applied at the exposed electrode is positive and the lower electrode is grounded, $\partial\phi/\partial x$ is negative. Therefore the *x* component of the electric field E_x is positive. From Eq. 10, we have $\rho_c > 0$ since ρ_c is synchronized with ϕ. This results in $f_{b,x} > 0$, that is the *x* component of the body force vector from Eq. 11 is in the positive *x* direction. This is in agreement with the experimental observations. A similar analysis for the case shown in Fig. 4b (when a negative voltage is applied at the exposed electrode) results in the same conclusion: *x* component of the body force vector is in positive *x* direction. This is in accordance to what was observed experimentally.

The boundary conditions and the computational domains of Eqs. (8) and (10) for a single pair of electrodes are shown in Figures 5a and 5b, respectively. Equation (8) is solved for the electric potential, ϕ, imposing the applied

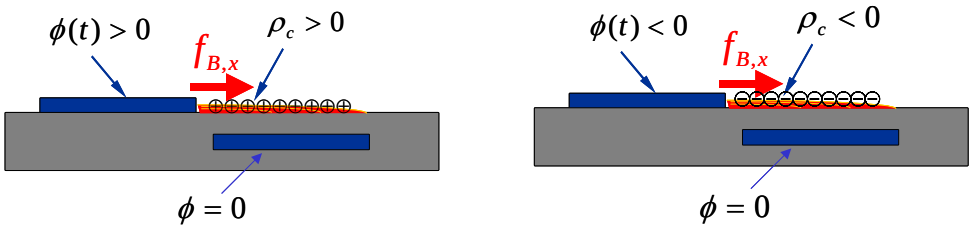

(a) Positive voltage at the upper electrode **(b) Negative voltage at the upper electrode**

Figure 4. Body force and flow directions using Eqs. (8), (10), and (11).

voltage on the electrodes as boundary conditions and using the appropriate ε_r value on both the air side and the wall. For air, $\varepsilon_r = 1.0$ and the experiments we considered for test cases used Kapton as the dielectric material which has an ε_r value of 2.7. On the wall-air interface harmonic mean of ε_{r1} and ε_{r2} must be used in order to conserve electric field[15].

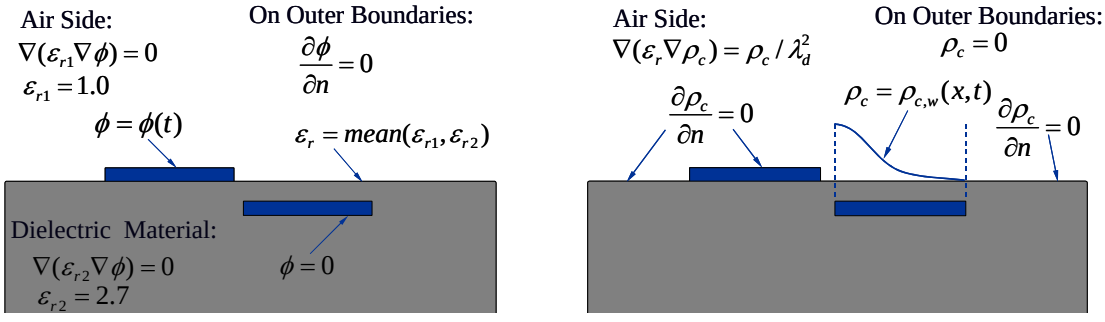

(a)Boundary conditions for Eq. (8) **(b) Boundary conditions for Eq. (10)**

Figure 5. Boundary conditions and computational domain for Eqs. (8) and (10).

Applied AC voltage imposed at the exposed (upper) electrode as boundary condition is:

$$\phi(t) = \phi^{\max} f(t) \tag{12}$$

The wave form function, $f(t)$, can be a sine wave given by:

$$f(t) = \sin(2\pi\omega t) \tag{13}$$

where ω is the frequency and $\phi^{\max}$ is the amplitude, both of which are known quantities from experiment. The embedded electrode is prescribed as ground by setting the electric potential to zero on that electrode. At the outer boundaries, $\partial\phi/\partial n = 0$ is assumed as shown in Figure 5a.

Eq. (10) with the boundary conditions shown in Fig. 5b being imposed is solved only on the air side to obtain for the net charge density, ρ_c. A zero normal gradient for the net charge density is imposed on the solid walls except in the region covering the lower electrode. The charge density is set to zero on the outer boundaries. On the wall downstream of the exposed electrode where the embedded electrode is located, the charge density is prescribed in such a way that it is synchronized with the time variation of the applied voltage $\phi(t)$ on the exposed electrode, $f(t)$ in equation (12):

$$\rho_{c,w}(x,t) = \rho_c^{\max} G(x) f(t) \tag{14}$$

where $\rho_c^{\max}$ is the maximum value of the charge density allowed in the domain (in Coulomb/m^3) and is a parameter to be determined later. The variation of the charge density on the wall, $\rho_{c,w}$, in the streamwise direction, *x*, is prescribed by a function *G(x)* chosen to resemble the plasma distribution over the embedded electrode. Experimental results[16,18,19] suggest that this distribution is similar to a half Gaussian distribution given by

$$G(x) = \exp\left[-(x-\mu)^2/(2\sigma^2)\right] \tag{15}$$

for $x \geq 0$. In equation (15) μ is the location parameter indicating the *x* location of the maximum, and σ is a scale parameter determining the rate of decay. In the computations we have chosen the location parameter μ such that the peak corresponds to the left edge of the embedded electrode as shown in Figure 5b. Moreover, we have assumed that σ takes a value of 0.3 to allow a gradual decay of the charge density distribution from the left edge to the right edge.

At this stage, it should be noted that in order to solve Eq. (10) we need to specify two parameters, namely, $\rho_c^{\max}$ and λ_d. These parameters control the strength of the plasma actuator's effects on the flowfield and extent of these effects into the flowfield. These two parameters will have to be calibrated using available experimental data.
It should be also noted that, Eqs. (8) and (10) need to be solved only once at the beginning of Navier Stokes computations since these equations do not contain a time derivative term. This can be achieved by writing these equations in nondimensional forms as illustrated in Figs. 6a and 6b. The quantity ϕ can be normalized by the value of AC voltage of the exposed electrode, $\phi(t)$, in equation (12). Equation (8) can then be solved by imposing a constant boundary condition equal to unity at the upper electrode. Once the dimensionless ϕ distribution is

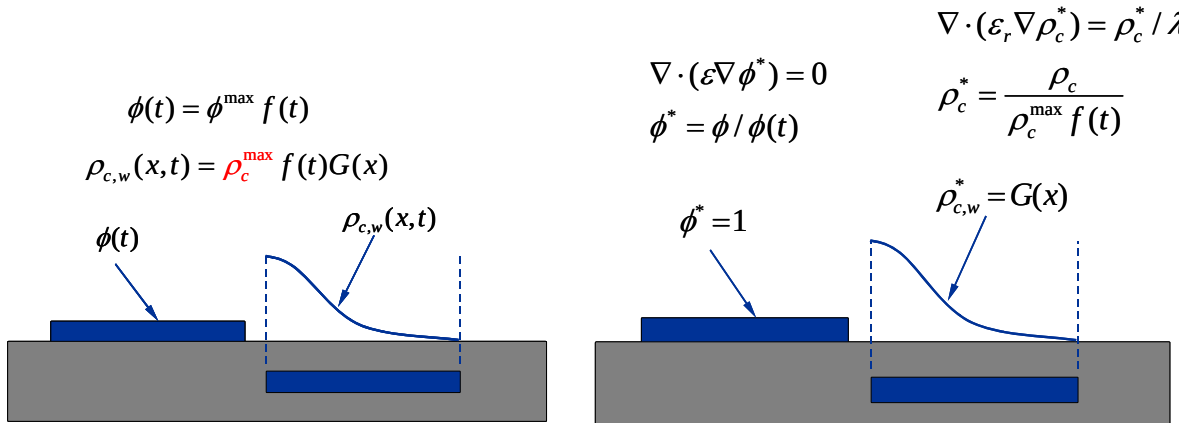

(a) Dimensional variables **(b) Nondimensional forms of Eqs. (8) and (10)**

Figure 6. Dimensional and nondimensional variables and nondimensional form for Eqs. (8) and (10).

determined, the dimensional ϕ values at any given time can be obtained by multiplying this distribution with the corresponding value of $\phi(t)$ given by equation (12). Similarly, Eq. (10) can be solved only once at the beginning of computations by using the dimensionless equation for the charge density distribution, which is normalized by $\rho_c^{\max} f(t)$. This implies that the boundary condition for the dimensionless charge density on the wall region covering the embedded electrode is *G(x)*. Once the solution for the dimensionless charge density is established, the dimensional values at any time can be calculated from this distribution by multiplying it with the corresponding value of $\rho_c^{\max} f(t)$.

This modeling approach for plasma actuators is implemented in the GHOST code developed at University of Kentucky. GHOST is a pressure-based code based on SIMPLE algorithm with second order accuracy in both time and space. This code is capable of handling complex geometries, moving and overset grids, and includes multiprocessor computation capability using MPI. The overset grid capability of the code enables incorporation of plasma actuators into the computations with relative ease since electrodes can be defined as individual solid blocks. The domain can be divided into two separate computational domains: one for the air side and the other for the dielectric wall. The GHOST code has been previously validated against a wide range of test cases and flow conditions and has been used extensively in several low pressure turbine related publications.[20,21]

III. Model Calibration and Validation

In order to calibrate the parameters Debye length, λ_d, and the maximum charge density on the wall, $\rho_c^{\max}$, appearing in the model we employed the quiescent flow experiments (Ref 22) conducted using a single pair of electrodes to better isolate the effects of the actuator on the surrounding air.[15] The details of the actuator geometry and experimental set up are given in Reference [15]. The actuator consists of two 10mm wide, 0.102mm thick conductive copper strips as electrodes which are separated by a 0.127mm thick Kapton dielectric with a ε_r value of 2.7. Streamwise spacing of electrodes is 0.5mm.

In the experiments the lower electrode was grounded and plasma region was generated using a square wave with frequency of, $\omega = 4.5\,\text{kHz}$ and amplitude of $\phi^{\max} = 5\,\text{kV}$. It should be noted that the experimental data is preliminary and it is used here only to demonstrate the proof of concept for the modeling approach. In the computations our aim was to match the maximum velocity observed in the experiments as well as the experimentally observed flow pattern shown in Figure 7a. From the experiment it was observed that the flow was drawn into the surface region above the embedded electrode by the plasma induced body force. This resulted in a jet issuing to the right of the actuator with a maximum velocity of approximately 1 m/s.

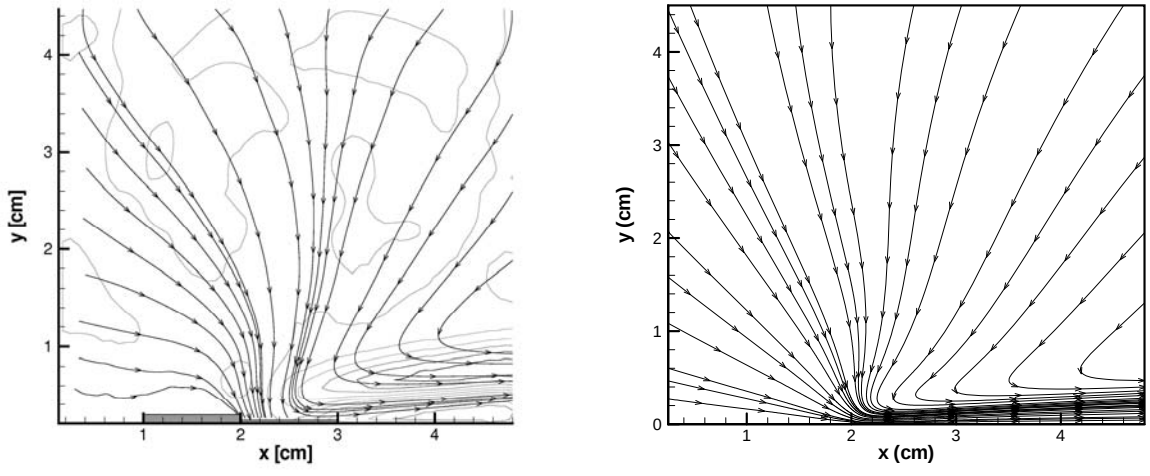

(a) Experiment[22] **(b) Computation**

Figure 7. Comparison of experimental[22] and computed streamlines for the plasma actuator in quiescent flow (The actuator interface is located at the 2cm tick.)

Based on the flow pattern and maximum velocity criteria, a choice of the parameter values of λ_d =0.001m and ρ_c^{max} =0.0008C/m^3 seems to agree well with the experiment. The streamlines obtained from the computation using these values are shown in Figure (7b). Although not an exact match, the computed flow pattern compares favorably with the experimental flowfield shown in Figure (7a). The computed maximum velocity is 1m/s also matching the experimental value. It should be noted that the boundary layer obtained by the computation appears to be thinner than the experimental data. Although the thickness could be adjusted by increasing the value of the Debye length, λ_d, we did not attempt to do so because the experimental data may be contaminated by 3-D effects caused by the experimental setup.

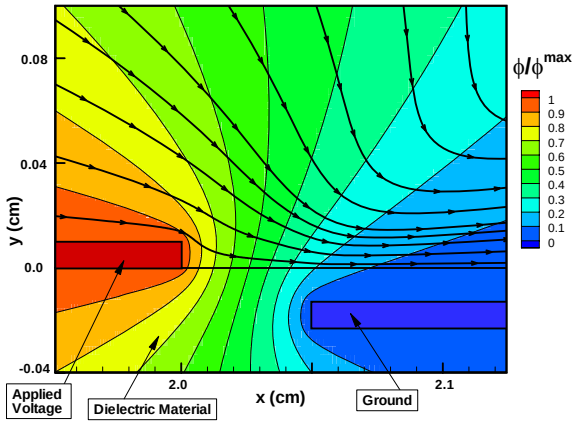

Figure 8. Computed electric potential contours and streamlines in the vicinity of the electrodes

The computed electric potential distribution in the vicinity of the electrodes obtained from equation (8) is shown in Figure 8 along with the streamlines of the actuator induced flow. The computed electric potentials show that the strongest electric potential variation, or the electric field, is in the region between the two electrodes. This is also the region where the strongest concentration of plasma is observed in the experiments. The streamlines indicate that the flow is pulled from above into this region and jetted to the right direction as observed experimentally.

IV. Flow Separation Control over a PAK-B Low-Pressure Turbine Blade

In order to illustrate the new models applicability to plasma flow control applications a representative case from the experiments of Huang et al[1] is selected. Huang et al[1] conducted experiments on PAK-B blade cascade for a range of Reynolds numbers and turbulence intensities. The Reynolds numbers range from 10,000 to 100,000 based on inlet velocity and axial chord. The freestream turbulence intensity in the tunnel was measured as 0.08%. In experiments separation control was performed using different configurations of plasma actuators. The tested configurations included a single spanwise actuator, dual spanwise actuators, and streamwise actuators. The spanwise actuators were designed to produce wall-directed jets and the streamwise actuators were designed to produce streamwise vortices. The results of the experiments demonstrated the effectiveness of plasma actuators in flow separation control at different freestream conditions.

We selected an intermediate case from the available Reynolds number range for demonstration purposes because it has a large flow separation region and the experimental data taken includes velocity profiles at various stations on the suction side of the blade and the pressure coefficient distribution. The flow conditions are Re= 50,000 based on cascade inlet velocity and axial chord length and the freestream turbulence intensity is 0.08%. The experimental data for the base flow without flow control was used for comparison. The flow separation zone is characterized by the plateau in the Cp distribution on the suction side of the blade. It is observed experimentally that the separation for the no-actuator flow extends from $x/C_x \approx 0.7$ to 0.95, as shown in Figure 9. Figure 9 also shows the comparison of the C_p distribution on the surface of the blade from the computation. The results show the separation starts at $x/C_x \approx 0.7$ but ends slightly earlier than the experimental location.

The same actuator configuration as discussed in section III is introduced on the suction surface of the blade with actuator interface located at 65% axial chord. Note that the actuator that was used in the simulation is not identical to the actuator used in Huang et al.[9] A sine wave voltage with a frequency of 5kHz, and an amplitude of 5kV is applied in the current demonstration. As can be seen from Figure 9, the use of the plasma actuator has caused the separation to reduce in size. The comparison of velocity profiles at various stations on the suction surface of the blade is shown in Figure 10. The figure shows that the size of the separation is reduced to end at $x/C_x \approx 0.87$. The ability of the model to simulate a control of flow separation for a low pressure turbine blade is demonstrated.

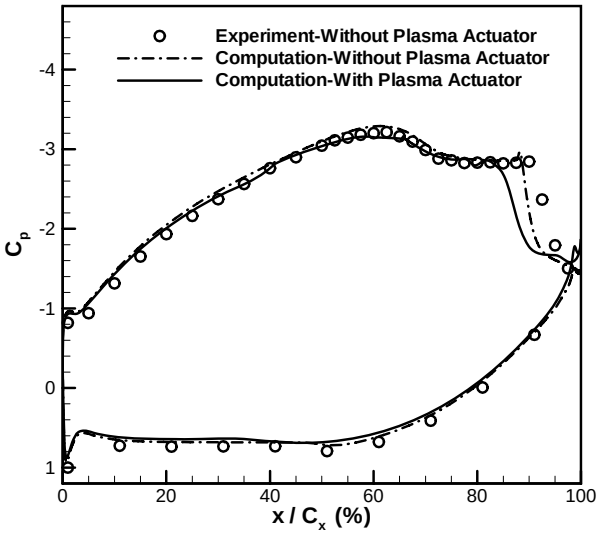

Figure 9. Comparison of pressure coefficient distribution for Pak-B Blade, Re=50,000, FSTI=0.08%.

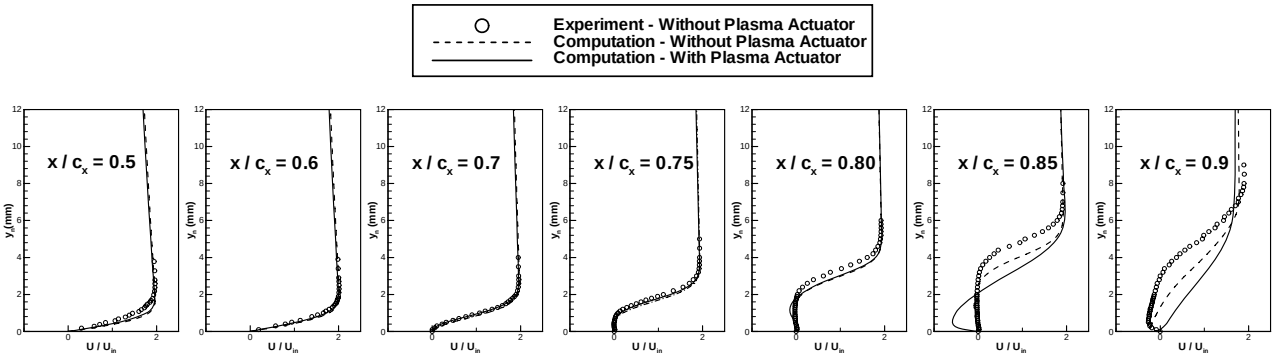

Figure 10. Comparison of velocity profiles for Pak-B Blade, Re=50,000, FSTI=0.08%.

V. Concluding Remarks

A new modeling approach for simulation of flow control applications using plasma actuators is outlined. The model solves two additional equations representing electrical field and charge density of the ionized air, only once before the Navier-Stokes computations. A body force vector is calculated from the solutions of these two quantities and incorporated into Navier-Stokes equations to account for the plasma-actuator effects. The model is calibrated against a simple plasma-actuator-driven flow in a quiescent environment. The model is then used to simulate an actual low-pressure turbine flow to achieve reduction of flow separation. The results indicated that the model can mimic the experimentally observed effects caused by plasma actuators and illustrated that the model and the approach are promising in the computation of plasma flow control applications.

Acknowledgments

This work is supported by NASA-Glenn Research Center under Cooperative Agreement NCC3-1040.

References

[1] Huang, J., Corke, T.C., Thomas, F.O., 2003, "Plasma Actuators for Separation Control of Low Pressure Turbine Blades,"AIAA-2003-1027, AIAA 41st Aerospace Sciences Meeting and Exhibit, Reno, NV, January 2003.

[2] Roth, J.R., Sherman, D.M., Wilkinson, S.R., 2000, "Electrohydrodynamic Flow Control with a Glow-Discharge Surface Plasma," AIAA Journal, Vol. 38, No. 7, July 2000.

[3] Corke, T., Cavalieri, D., Matlis, E., 2001, "Boundary Layer Instability on a Sharp Cone at Mach 3.5 with Controlled Input," AIAA Journal, Vol. 40, No 5., pp. 1015.

[4] Corke, T., Jumper, E., Post, M., Orlov, D., McLaughlin, T., 2002, "Application of Weakly ionized Plasmas as Wing Flow Control Devices," AIAA-2002-0350.

[5] Post, M.L., Corke, T., 2003, "Separation Control on High Angle of Attack Airfoil Using Plasma Actuators," AIAA 2003-1024.

[6] Hultgren, L.S., Ashpis, D.E., 2003, "Demonstration of Separation Delay with Glow-Discharge Plasma Actuators," AIAA-2003-1025. Reno, NV, Jan. 2003.

[7] Jacob, J., Rivir, R., Campbell, C., Estevedoreal, J., 2004, "Boundary Layer Flow Control Using AC Discharge Plasma Actuators." AIAA-2004-2128, 2nd Flow Control Conference, Portland, OR.

[8] Post, M.L., Corke, T., 2004, "Separation Control Using Plasma Actuators- Stationary & Oscillating Airfoils," AIAA-2004-0841.

[9] Morris, S.C., Corke, T.C., VanNess, D., Stephens, J., Douville, T., "Tip Clearance Control Using Plasma Actuators,", AIAA-2005-0782, January 2005.

[10] Shyy, W. Jayaraman, B., Andersson, A., "Modeling of Glow Discharge-Induced Fluid Dynamics," Journal of Applied Physics, Vol. 92, No. 11, pp. 6434-6443, December 2002.

[11] Hall, K.D., Jumper, E.J., Corke, T.C., McLaughlin, T.E., "Potential Flow Model of a Plasma Actuator as a Lift Enhancement Device," AIAA-2005-0783, January 2005.

[12] Orlov, D.M., Corke, T.C., "Numerical Simulation of Aerodynamic Plasma Actuator Effects," AIAA 2005-1083.

[13] Roy, S., Gaitonde, D., "Radio Frequency Induced Ionized Collisional Flow Model for Application at Atmospheric Pressures,", Journal of Applied Physics, Vol. 96, No. 5, pp. 2476-2481, September 2004.

[14] Roy, S., Gaitonde, D., "Modeling Surface Discharge Effects of Atmospheric RF on Gas Flow Control," AIAA-20050160, January 2005.

[15] Suzen, Y.B., Huang, P.G., Jacob, J.D., Ashpis, D.E., "Numerical Simulations of Plasma Based Flow Control Applications,: AIAA-2005-4633, June 2005, Toronto, Ontario.

[16] Enloe, C.L., McLaughlin, T.E., VanDyken, R.D., Kachner, K.D., Jumper, E.J., Corke, T.C., Post, M., Haddad, O., 2004, "Mechanisms and Responses of a Single Dielectric Barrier Plasma Actuator: Geometric Effects," AIAA Journal, Vol. 42, No. 3, pp. 595-604, March 2004.

[17] Patankar, N. A., Hu, H.H., "Numerical Simulation of Electroosmotic Flow," Analytical Chemistry, Vol. 70, No. 9, pp. 1870-1881, May, 1998.

[18] Enloe, C.L., Mclaughlin, T.E., Font, G.I., Baughn, J.W., "Parameterization of Temporal Structure in a Single Dielectric Barrier Aerodynamic Plasma Actuator," AIAA-2005-0564, January 2005.

[19] Enloe, C.L., Mclaughlin, T.E., VanDyken, R.D., Fischer, J.C., "Plasma Structure in the Aerodynamic Plasma Actuator," AIAA-2004-0844, January 2004.

[20] Suzen, Y.B., Huang, P.G., "Numerical Simulation of Unsteady Wake/Blade Interactions in Low Pressure Turbine Flows Using an Intermittency Transport Equation," *Journal of Turbomachinery*, Vol. 127, No. 3, pp. 431-444, July 2005.

[21] Suzen, Y.B., Huang, P.G., "Comprehensive Validation of an Intermittency Transport Model for Transitional Low-Pressure Turbine Flows," *The Aeronautical Journal*, Vol. 109, No. 1093, pp. 101-118, March 2005.

[22] Jacob, J.D., Ramakumar, K., Anthony, R., Rivir, R.B., "Control of Laminar and Turbulent Shear Flows Using Plasma Actuators," Fourth International Symposium on Turbulence and Shear Flow Phenomena, TSFP-4, Williamsburg, VA, June 2005.